Early Pleistocene drainage pattern changes in Eastern Tibet: Constraints from provenance analysis, thermochronometry, and numerical modeling

Author(s):
Yang, Rong; Suhail, Hakro A.; Gourbet, Loraine; Willett, Sean D.; Fellin, Maria Giuditta; Lin, Xiubin; Gong, Junfeng; Wei, Xiaochun; Maden, Colin; Jiao, Ruohong; Chen, Hanlin

Publication date:
2020-02-01

Permanent link:
https://doi.org/10.3929/ethz-b-000391566

Originally published in:
Earth and Planetary Science Letters 531, https://doi.org/10.1016/j.epsl.2019.115955

Earth and Planetary Science Letters 531 (2020) 115955

Contents lists available at ScienceDirect

Earth and Planetary Science Letters

www.elsevier.com/locate/epsl

Early Pleistocene drainage pattern changes in Eastern Tibet: Constraints from provenance analysis, thermochronometry, and numerical modeling

Rong Yang [a,*], Hakro Ahmed Suhail [a], Loraine Gourbet [b], Sean D. Willett [b], Maria Giuditta Fellin [b], Xiubin Lin [a], Junfeng Gong [a], Xiaochun Wei [a], Colin Maden [b], Ruohong Jiao [c], Hanlin Chen [a]

[a] School of Earth Sciences, Zhejiang University, 310027 Hangzhou, China
[b] Department of Earth Sciences, ETH Zürich, 8092 Zürich, Switzerland
[c] Helmholtz Centre Potsdam, GFZ German Research Centre for Geosciences, Telegrafenberg, 14473 Potsdam, Germany

ARTICLE INFO

Article history:
Received 16 May 2019
Received in revised form 31 October 2019
Accepted 5 November 2019
Available online 18 November 2019
Editor: A. Yin

Keywords:
eastern Tibet
river capture
provenance analysis
thermochronometry
river analysis
numerical modeling

ABSTRACT

The geometry and evolution of fluvial systems are thought to be related to surface uplift. In eastern Tibet, rivers exhibit peculiar drainage patterns but how these patterns were established and their connection with the plateau uplift are still under debate. Here, we use detrital zircon U-Pb dating, bedrock (U-Th)/He thermochronometry, topographic analysis and numerical modeling to explore the paleo-drainage pattern of the Dadu and Anning Rivers, eastern Tibet. Our detrital data indicate that the Pliocene sources of sediments to the Anning River are different from the modern ones and they include a source similar to that of the modern Dadu River, implying a paleo-connection between the Dadu and the Anning Rivers and a subsequent cutoff of this connection after the deposition of the Pliocene sediments. Bedrock thermochronometric data along the Dadu River reveal rapid cooling at ~10 Ma and a possible enhanced cooling at ~2 Ma, which we interpret as a response to the regional plateau uplift in eastern Tibet and to the Dadu-Anning capture, respectively. Combined with topographic analysis and numerical modeling, our results indicate an Early Pleistocene capture between the Dadu and Anning Rivers, resulting in the changes in the sediment sources of the Anning River, enhanced incision of the Dadu, and the transience of the Dadu River profile. The Dadu-Anning capture is related to the motion along the active sinistral strike-slip Daliangshan fault that locally disrupts the river network. This event does not date the plateau uplift; rather, it indicates how river reorganization can effectively enhance river incision and affect landscape development independently from regional-scale uplift.

1. Introduction

The development of fluvial systems is closely linked to the evolving topography and thus to surface uplift in tectonic active region. Hence, river channels and their map-pattern geometry and elevation profiles are useful geomorphic features that can be used to infer tectonic deformation. In the eastern Tibetan Plateau, the Yangtze River and its main tributaries, including the Yalong and the Dadu Rivers, exhibit unusual channel patterns with sudden changes in their flow paths (Fig. 1a). Such river geometries have been proposed to result from river rerouting in response to plateau uplift (Barbour, 1936; Brookfield, 1998; Clark et al., 2004). However, lines of evidence for river rerouting, its timing and causes are still debated (Clark et al., 2004; Clift et al., 2006; Gourbet et al., 2017; Kong et al., 2009, 2012; Wei et al., 2016; Yan et al., 2012; Zhang et al., 2017b, 2019).

Most of the previous studies focus on the upper Yangtze River diversion and the formation of the Yangtze "First Bend" (Fig. 1a). Clark et al. (2004) proposed a capture of the upper Yangtze River from the Red River prior to or coeval with the initiation of Miocene plateau uplift. In contrast, detrital zircon U-Pb dating on sediments from the Jianchuan basin (Fig. 1a) immediately south of the Yangtze "First Bend" suggests the establishment of the modern upper Yangtze River since Late Oligocene associated with regional strike-slip faulting (Yan et al., 2012). However, Wei et al. (2016) reevaluated the sedimentary facies in the Jianchuan basin

* Corresponding author.
E-mail address: royang1985@zju.edu.cn (R. Yang).

https://doi.org/10.1016/j.epsl.2019.115955

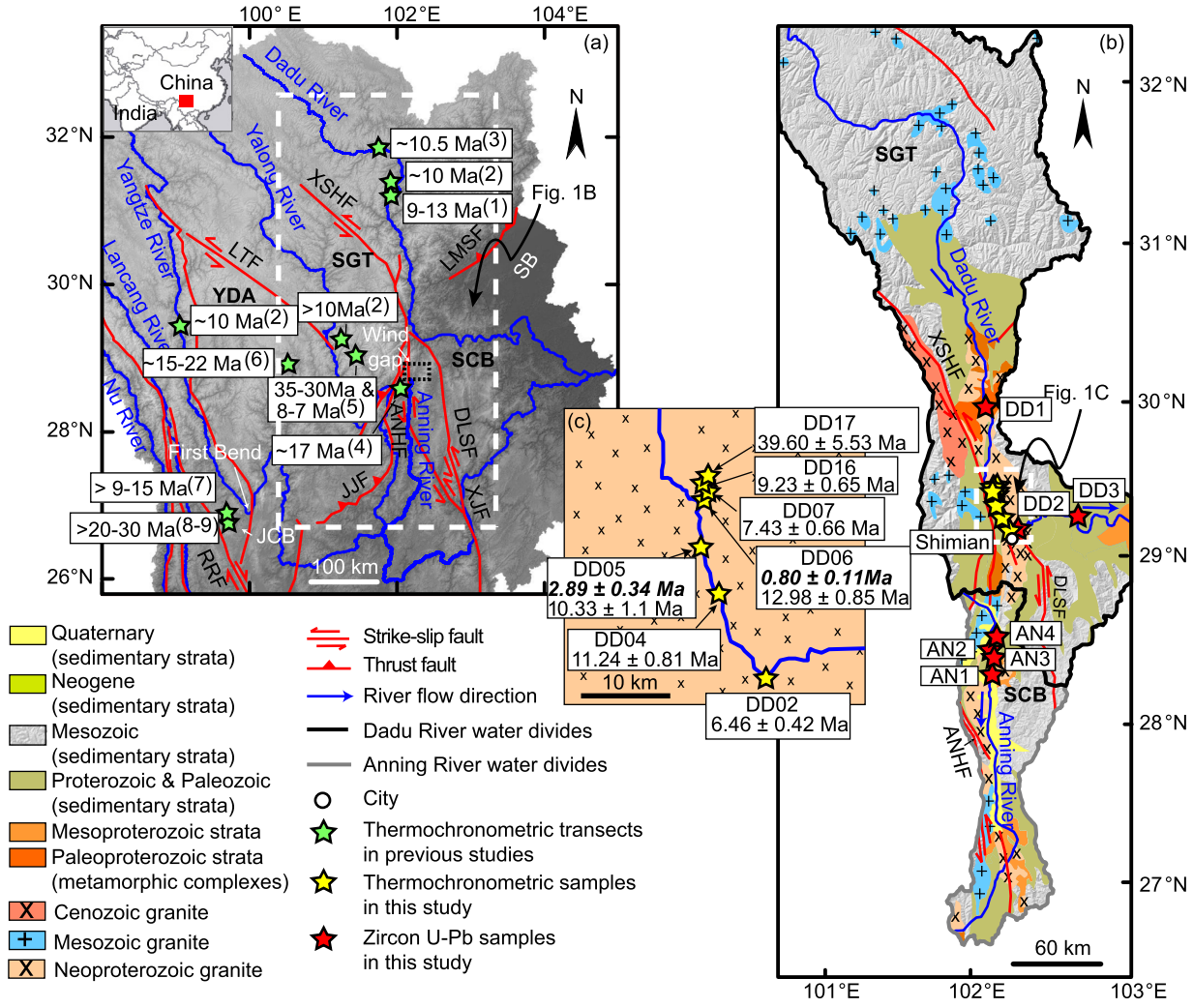

Fig. 1. Geological and tectonic settings of eastern Tibet. (a) Topography, active faults, and major rivers in the eastern Tibetan Plateau. Green stars indicate estimates for the onset of rapid cooling along rivers compiled from (1)-Clark et al., 2005; (2)-Ouimet et al., 2010; (3)-Tian et al., 2015; (4)-Wang et al., 2012; (5)-Zhang et al., 2016; (6)-Tian et al., 2014; (7)-Mcphillips et al., 2015; and (8)-Shen et al., 2016, (9)-Cao et al., 2019. (b) Simplified regional geologic map of the Dadu River and Anning River drainage basins (base map from SBGMR, 1991). Yellow stars show samples collected for thermochronometric analysis and red stars show samples collected for zircon U-Pb measurement in this study. (c) Sampling sites and mean AHe (bold italic) and ZHe ages from this study. RRF: Red River fault; JJF: Jinhe-Jianhe fault; LTF: Litang fault; XSHF: Xianshuihe fault; ANHF: Anninghe fault; DLSF: Daliangshan fault; XJF: Xiaojiang fault; LMSF: Longmenshan fault; YDA: Yindun Arc; SGT: Songpan-Ganze Terrane; SCB: South China Block; JCB: Jianchuan Basin; SB: Sichuan Basin. (For interpretation of the colors in the figure(s), the reader is referred to the web version of this article.)

and found that these sediments were locally sourced, thus preserving no information of the paleo-drainage configuration. A recent study suggested a disconnection between the Yangtze and the Red Rivers at the end of the Eocene after revising the stratigraphy and the depositional ages in that basin (Gourbet et al., 2017).

In contrast to the Yangtze main trunk, less attention has been paid to the diversion of its major tributaries. The Dadu River, located to the west of the Sichuan basin, originates from the Songpan-Ganze Terrane and flows in a north-south direction in its upper course. Near the eastern boundary of the Tibetan plateau (at the town of Shimian), this river makes an abrupt 90° turn and flows eastwards into the Sichuan Basin (Fig. 1b). The abrupt change in the river course occurs adjacent to a low, wide pass (Fig. 1a) that separates the north-south course of the Dadu River from the headwaters of the north-south oriented Anning River. The Anning River flows southward in a broad, alluviated valley with gentle river gradients in the upper reaches and becomes gradually entrenched downstream before joining the Yangtze River. The entire watershed of the Anning River is within the western South China Block (Fig. 1b). Portions of both the Anning and Dadu river courses are parallel to active faults, including the Xianshuihe fault and the northern end of the Daliangshan fault near the Dadu turn and the Anninghe fault along the upper reaches of the Anning River. Both the N-S trending Anninghe fault and the NNW-SSE trending Daliangshan fault are major sinistral faults located at the connection zone between the NWW trending left-lateral Xianshuihe fault and the N-S trending left-lateral Xiaojiang fault (Fig. 1a). Previous studies have proposed the existence of a S-flowing paleo-Dadu-Anning River through the wide pass and a subsequent river capture of the upper reaches of this paleo-river near Shimian in response to the Tibetan Plateau uplift (Clark et al., 2004). The map patterns, the existence of the wide pass (wind gap) that separates the N-S portion of the Dadu from the headwaters of the Anning and fluvial sediments preserved in the wind gap argue for the capture (Clark et al., 2004), however, the timing of the capture and the consequences for the geomorphology of the impacted valleys remain open questions.

In this study, we investigate the changing drainage pattern of the Dadu and Anning Rivers using a multi-disciplinary approach including provenance analysis, thermochronometry, topographic analysis and numerical modeling. These different approaches allow exploring both passive (provenance) and active (fluvial in-

cision) recorders of drainage reorganization. For instance, provenance analysis by detrital zircon U-Pb dating of sediments with known depositional age is used to constrain a possible change in the source areas of the fluvial deposits, which should follow the capture from the Anning to the Dadu River. Low-temperature thermochronometry together with topographic analysis and numerical modeling is applied to investigate and simulate the river capture to test patterns and extent of incision on the capturing reaches. Incision should result from the increased discharge and sediment flux of the river downstream of the capture location and it should propagate through the catchment (Yanites et al., 2013). Thus, the combination of all these approaches should provide comprehensive constraints on the drainage pattern change.

2. Provenance analysis and drainage reorganization

In order to reconstruct the configuration of the paleo-drainage network of the Dadu and Anning Rivers, we collected present-day and paleo-fluvial sediments to trace the sources of the sediments. We collected three sand samples from the modern Dadu River channel: one located at Shimian and the other two about 80 km in the upstream and 50 km in the downstream from Shimian, respectively (Fig. 1b, Supplementary Data Table 1). We also collected two sand samples from the upper reaches of the Anning River, and two samples from the Xigeda Formation that outcrops along the eastern bank of the Anning River (Fig. 1b, Supplementary Data Table 1). This formation is characterized by fluvial-lacustrine facies and is widely distributed along the upper Yangtze River channel and its major tributaries: the Yalong, Anning, and Dadu Rivers (Jiang et al., 1999; Kong et al., 2009; Qian et al., 1984; Yao et al., 2007). Due to the lack of fossils in this formation, these deposits have been dated by magnetostratigraphic (Qian et al., 1984; Wang et al., 2006; Jiang et al., 1999; Yao et al., 2007) and cosmogenic nuclides methods (Kong et al., 2009) which give spatially comparable ages of late Pliocene to early Pleistocene. Along the Anning River, this formation is ~300 m thick and it unconformably overlies the Pre-Sinian metamorphic rocks and underlies the conglomerates of the modern Anning River terrace deposits (Yao et al., 2007). Electron spin resonance (ESR) dating on these conglomerates provides an upper limit for the depositional age of this formation before ~1.3 Ma (Yao et al., 2007). The magnetostratigraphy of this formation shows three normal and three reverse chrons which have been correlated to the time period between ~4.2 to 2.6 Ma (Yao et al., 2007).

We performed U-Pb dating on detrital zircon grains from these sediments. Zircon grains were extracted from these samples following conventional heavy liquid and magnetic separation procedures. Each sample was then analyzed by zircon U-Pb dating method (Supplementary Data Table 2). Fig. 2a-g shows the age distributions of all the samples. There are three main age populations centered at 205-215 Ma, 447-459 Ma and 766-789 Ma, respectively. The 447-459 Ma population is present in the two samples from the Xigeda Formation (AN3 and AN4) and in the modern samples from the Dadu River (DD1 and DD2), where it appears as a small, smooth peak. The 205-215 Ma and 766-789 Ma peaks are present in all samples but with very different relative abundances. In the Dadu modern river samples (DD1-DD3) and in the Xigeda samples (AN3 and AN4), the 205-215 Ma peak is prominent and the 766-789 Ma peak is modest. In the modern Anning River, the relative abundance of these peaks is opposite to that of the Dadu River: the 205-215 Ma peak is modest and the 766-789 Ma peak is dominant.

We interpret the age spectra of the Dadu River samples as signatures of the Songpan-Ganze Terrane. In the upper reaches of the Dadu drainage basin, Triassic sediments are dominant with detrital zircon ages peaking at 229 Ma, 380 Ma, 719 Ma, 1860 Ma, and 2490 Ma (Ding et al., 2013; Enkelmann et al., 2007; He et al., 2014; Weislogel et al., 2006) (Fig. 2h) and Late Triassic-Early Jurassic volcanic rocks also occur (Roger et al., 2004; Yuan et al., 2010; Zhang et al., 2006) (Fig. 1b). In the lower reaches, Precambrian and Paleozoic rocks are exposed (Burchfiel and Chen, 2012) and Neoproterozoic granites with zircon U-Pb ages of 736-937 Ma (Shen et al., 2000) and Cenozoic granites with zircon U-Pb ages of ~13 Ma (Roger et al., 1995) are also present (Fig. 1b). By comparing the age populations of the modern Dadu samples with the Songpan-Ganze Terrane, we infer that the Triassic zircons in the modern sands are mainly from the upper Dadu drainage basin. Since the bedrock of the lower Dadu drainage basin also contains zircons of Neoproterozoic age, we cannot preclude that the lower Dadu also provides materials into the modern river. The absence of the Paleoproterozoic and Cenozoic ages in the modern Dadu River is probably due to dilution during sediment mixing, transport and deposition (Cawood et al., 2003) and poor fertility of zircons of the Cenozoic granites.

For the modern Anning River samples, we interpret the age spectrum with a major Neoproterozoic peak and a small Triassic peak as characteristic of the South China Block (Fig. 2i). In this region, Neoproterozoic U-Pb ages ranging from 743 to 1034 Ma are widespread in different types of rocks (He et al., 2014; Huang et al., 2009; Sun et al., 2009; Zhao and Zhou, 2007; Zhou, 2002). Locally, volcanic rocks associated with the Emeishan volcanism contain Triassic zircons (Xu et al., 2008).

The two samples from the Xigeda Formation are characterized by the dominance of Late Triassic materials over the Neoproterozoic materials. Although these two samples were collected close to the modern Anning River channel (AN3 was collected <1 km apart from AN2), their age spectra do not match with that of the modern Anning River samples. Rather, they share similarities with the Dadu River sample (DD1-DD3). This similarity suggests an identical source region for the Xigeda samples and the modern Dadu River samples from the Songpan-Ganze Terrane (Fig. 2). Likely, the absence of the Paleoproterozoic and Cenozoic ages in the Xigeda Formation also implies the effect of dilution on the paleo-sediments. We suggest that the sediments in the Xigeda Formation were transported from the upper Dadu River and a paleo-connection existed between the upper Dadu and the Anning Rivers during the period of the Xigeda sedimentation. Changes in the sediment sources between the Xigeda Formation and the modern Anning Rivers require a subsequent cutoff of this connection. Thus, the age of the Xigeda Formation (~4.2 to 2.6 Ma, Yao et al., 2007) provides a lower boundary for the time of the cutoff, which must have occurred after 2.6 Ma. We use this time constraint in section 4 to model the evolution of the paleo-Dadu-Anning River.

3. Low-temperature thermochronometry and river incision

River capture associated with river network disruption is capable of generating rapid incision by increasing the discharge and sediment flux of the river downstream of the capture location. Such an event can induce a pulse of incision that can propagate through a catchment (Yanites et al., 2013). Thus, an increase in the incision rate is expected along the Dadu if such a major capture has occurred. In order to constrain the incision history of the Dadu River, 17 bedrock samples were collected within a horizontal distance of <25 km along the Dadu River close to Shimian from the same Neoproterozoic granites which were emplaced at ~786 Ma as constrained by zircon U-Pb dating (Shen et al., 2000) (Fig. 1b). These samples were located on one side of the Xianshuihe fault and no clear evidence of faulting was observed between samples during field investigation. Of these samples seven provided dat-

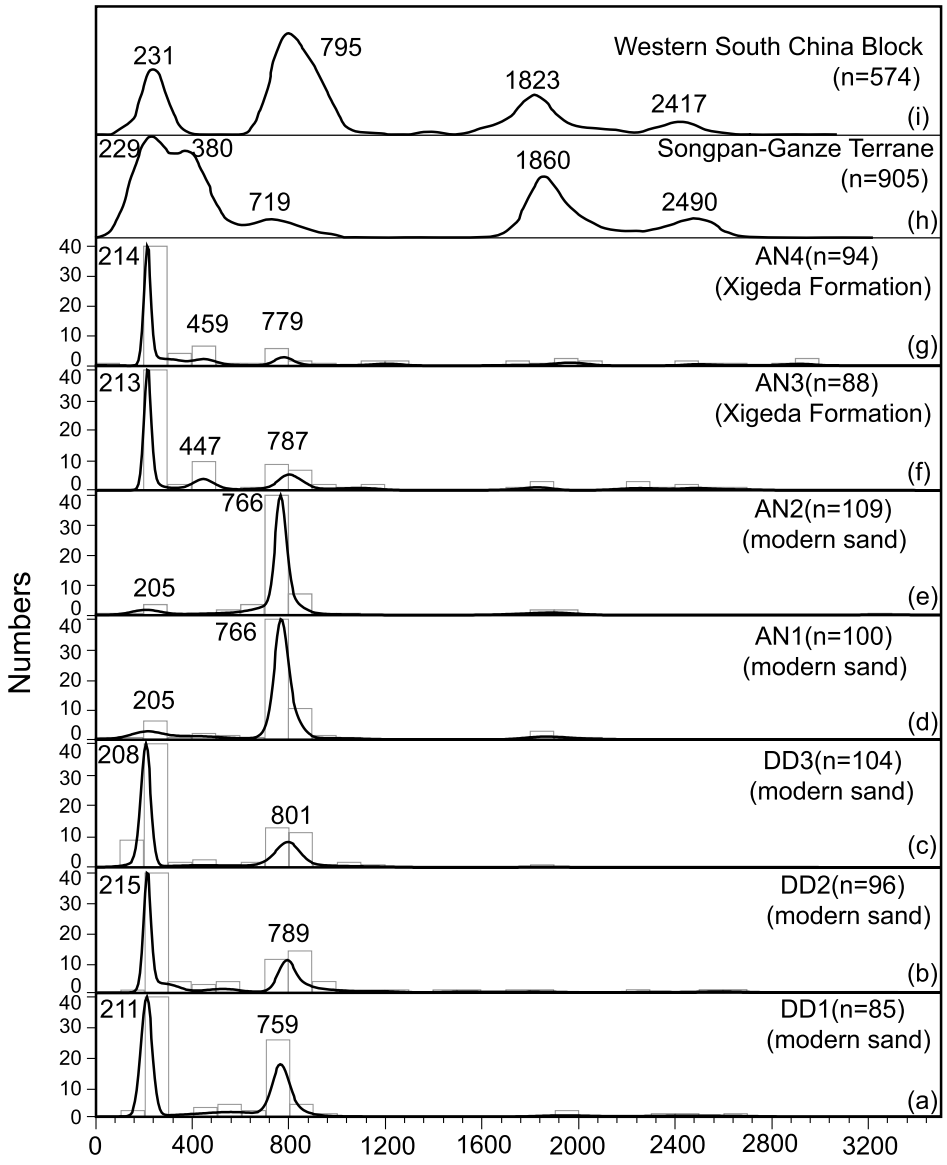

Fig. 2. Kernel Density Estimation (KDE) plots for the Zircon U-Pb ages of samples from this study (a-g) together with compiled ages in the Songpan-Ganze Terrane and Western South China Block (h-i) (He et al., 2014).

able zircon grains and two also provided datable apatite grains, on which we conducted (U-Th)/He dating. The elevations of the dated samples range from 874 to 2245 m (Fig. 3a). Apatite and zircon grains were separated by conventional heavy-liquid and magnetic separation procedures and handpicked.

The two apatite (U-Th)/He (AHe) ages are 0.8 ± 0.1 Ma and 2.9 ± 0.3 Ma, respectively (Fig. 1c, Supplementary Data Table 3). The highest elevation sample (DD17) yields a mean zircon (U-Th)/He (ZHe) age of 39.6 ± 5.5 Ma and the remaining samples yield ZHe ages ranging between 6.5 ± 0.4 and 13.0 ± 0.9 Ma (Fig. 1c, Supplementary Data Table 4). There is no clear correlation between sample elevations and ZHe ages (Fig. 3c) and a weak correlation between ZHe ages and effective uranium concentration (eU; Fig. 3d). The two oldest zircon grain ages have both a Th/U > 1 whereas all the other zircons have Th/U close to 0.5 (Fig. 3e). The independence of age on elevation could reflect high radiation damage in zircons combined with a long residence at shallow crustal levels before cooling below the closure temperature. Accumulation of radiation damage in zircons can cause an increase in helium diffusivity at high damage levels whereas at moderate levels, it can cause the opposite effect due to trapping of the decay products (Guenthner et al., 2013). The damage accumulation is governed by the U and Th concentration (expressed as eU) of the zircons, which can be highly variable, in combination with their cooling history because damage accumulation occurs at relatively low temperature.

We modeled our data with QTQt (Gallagher, 2012) a retention model that accounts for the effects of grain size, radiation damage and for the dependence of diffusivity on cooling rate. We used this model on samples located along a profile with an elevation offset of 1.2 km over a distance of 6 km and that includes four ZHe ages and one AHe age (Fig. 3a). We imposed an initial geothermal gradient of 30 °C/km, a surface temperature of 10 °C with an offset of 5 °C between top and bottom samples. We allowed the geothermal gradient to vary with time and no reheating: however, we modeled our data allowing reheating as well and this produces results that are not significantly different. Given that the observed ZHe and AHe ages vary between ≤1 Ma and 45 Ma and come from Neoproterozoic intrusive rocks, we provided two partly overlapping time-temperature constraints of temperatures between 200-10 °C over the last 60 Ma and 800-125 °C from 800 Ma to 30 Ma (Fig. 3f). Our modeling results suggest a long residence at tem-

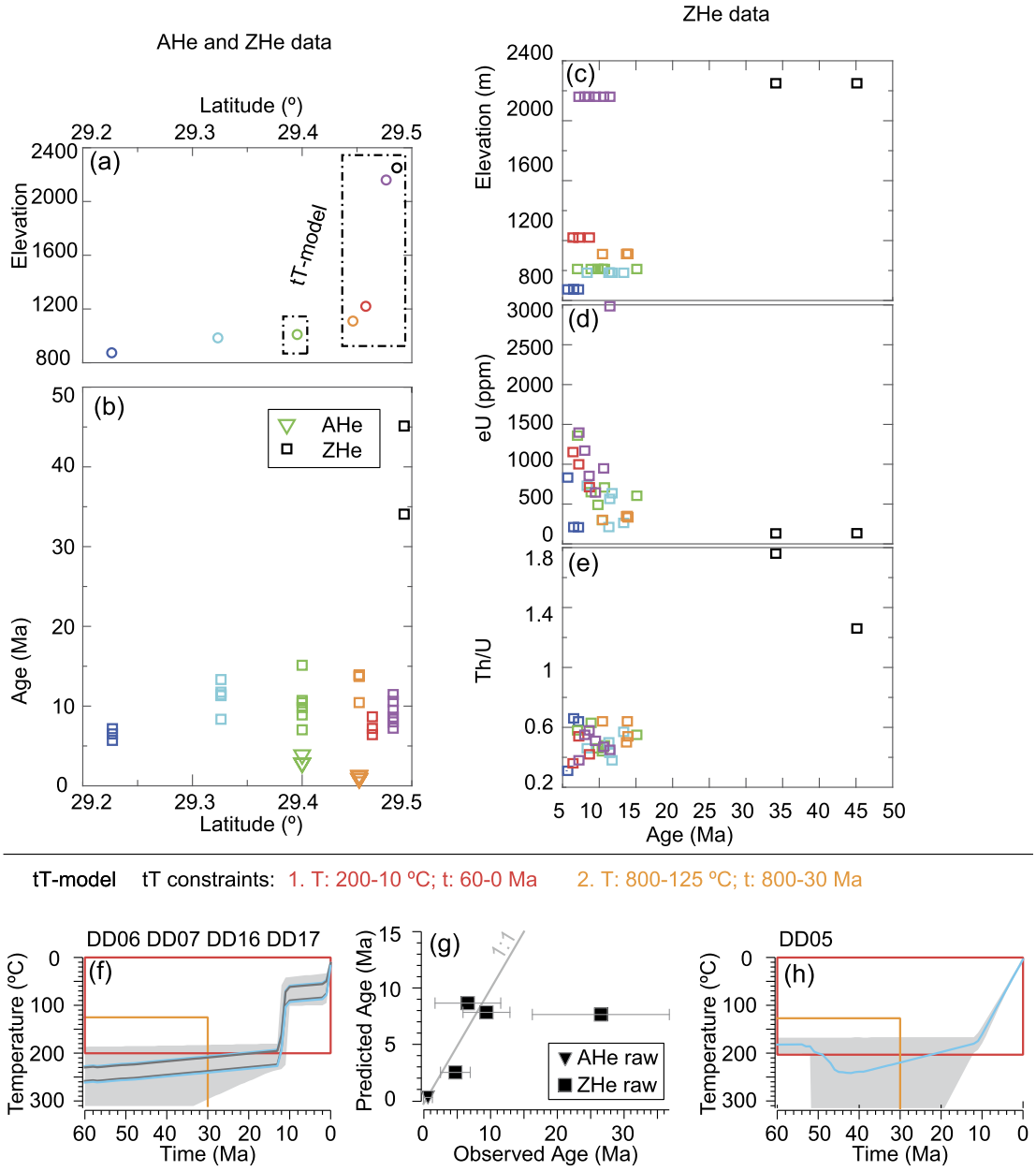

Fig. 3. Modeled thermal history using the QTQt software (Gallagher, 2012). (a) and (b) show plots of latitude against elevation of the samples and measured single grain AHe and ZHe ages, respectively. The two dashed boxes in (a) refer to the samples with the thermal histories modeled in (f) and (h). (c), (d), and (e) show plots of single grain ZHe ages against elevation, effective uranium concentration (eU), and U/Th, respectively. (f) shows the modeled thermal histories of sample DD06, DD07, DD16 and DD17. The light blue lines correspond to the thermal histories of the uppermost (DD17) and lowermost (DD06) samples and the grey lines show the thermal histories of the intermediate samples (DD07 and DD16). The grey envelope corresponds to the 95% confidence interval. (g) shows the observed AHe and ZHe mean ages against the modeled ones. (h) shows the modeled thermal history of sample DD05. The thermal history is depicted by the light blue line and the grey envelope represents the 95% confidence interval.

peratures close to 200-250 °C before 10 Ma and possible cooling pulses at ~10 Ma and at ~2 Ma (Fig. 3f). These results reflect the fact that most of the modeled ZHe ages vary around 10 Ma, the AHe ages are younger than 1 Ma and our oldest ages may have sampled the base of a fossil partial retention zone exposed at elevation ≥ 2250 m. The cooling pulse at ~10 Ma is supported also by the remaining ZHe data which range between 5 and 10 Ma. Our modeling can predict the AHe and ZHe ages ≤ 15 Ma but cannot reproduce the Eocene ZHe ages of the highest elevation sample (DD17; Fig. 3g). The inability of our modeling to reproduce the Eocene ZHe ages is likely due to the fact that these ages are from zircon grains with relatively low eU (<150 ppm) and that, as suggested by their high Th/U ratio, have unusual retention characteristics or thermal histories. We also modeled the only other sample that we could date with both systems, yielding a mean ZHe age of 10.3 ± 1.1 Ma and a mean AHe age of 2.9 ± 0.3 Ma (DD05, Fig. 3a). This sample suggests a near constant rate of cooling to the surface since ~10 Ma (DD05, Fig. 3h).

The rapid cooling initiated at ~10 Ma determined from our thermochronometric data in the Dadu River is consistent with the onset of rapid river incision in the upper reaches of the Dadu, >280 km to the north (Clark et al., 2005; Ouimet et al., 2010; Tian et al., 2015) (Fig. 1a, Supplementary Data Table 5), and is also consistent with the initiation of rapid exhumation in the Gongga Shan (Wilson and Fowler, 2011; Xu and Kamp, 2000; Zhang et al., 2017a) to the west of the Dadu River and in the Longmen Shan to the east (Godard et al., 2009; Kirby et al., 2002; Tian et al., 2013). Thus, we infer that the Late Miocene cooling in the Dadu River is

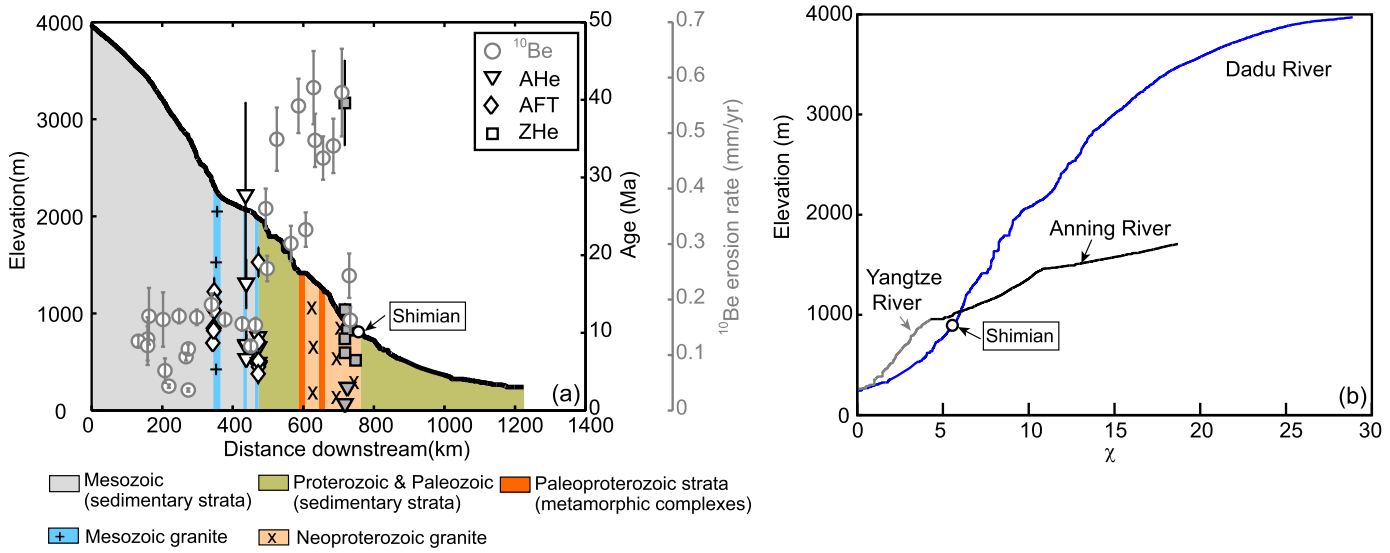

Fig. 4. The Dadu River longitudinal profile with bedrock lithology, the projected thermochronometric data from Clark et al. (2005), Ouimet et al. (2010), Tian et al. (2015), and this study (Supplementary Data Table 5) and the ^{10}Be-based erosion rates from Ouimet et al. (2009) (a) and the χ-plots for both the Dadu and Anning Rivers (b). Mean thermochronometric ages are shown and data from this study are filled in grey in (a).

related to rapid river carving in response to the regional plateau uplift. We find evidence of a second rapid cooling pulse at ~2 Ma. The fact that the youngest AHe ages (<1 Ma) are only observed in the lower Dadu (Fig. 4a) is consistent with our hypothesis that this is a rapid cooling phase associated with the Dadu-Anning river capture. It is clear that this cooling event is on the edge of resolvability given the few ages and the fact that exhumation in this event was limited, so our interpretation rests on the combination of observables.

4. River profile analysis and modeling

To examine the transient response to river capture, we analyzed the river profiles of the Dadu and Anning Rivers supplemented by numerical modeling of the Dadu channel profile. In bedrock rivers, the change in elevation, z, at a point, x, along a river is determined by rock uplift, U, and erosion rate which is a function of rock erodibility, K, drainage area, A, and channel slope, S, following a stream power law (Howard, 1994)

$$\frac{dz}{dt} = U(t) - KA^m S^n \quad (1)$$

where m and n are constants. The ratio (m/n) commonly ranges between 0.4-0.7 for equilibrium channels (Stock and Montgomery, 1999; Tucker and Whipple, 2002) and the slope exponent, n, ranges between 2/3 and 5/3 (Whipple et al., 2000). The river longitudinal profile can also be transformed into a scaled length dimension, χ, where χ is an integration of drainage area from the local base level (x_b) (Perron and Royden, 2012): $\chi = \int_{x_b}^{x} (\frac{A_0}{A(x)})^{\frac{m}{n}} dx$. The slope of this scaled longitudinal profile, (χ-plot: elevation against χ), is the channel steepness and should be proportional to erosion rate. As in Yang et al. (2015), we used an m/n of 0.45 in our model as this value minimizes the dispersion of the χ-plots for all the streams in the Yangtze drainage basin and an A_0 of 1 km^2. x_b was set at the confluence where the Dadu River joins the Yangtze River in the Sichuan Basin.

The Dadu and Anning river profiles were extracted from the SRTM3 DEM data (with a resolution of ~90 m). A drainage area of 1 km^2 was used to exclude the headwaters that are potentially affected by debris flows. The Dadu River longitudinal profile shows a steep, convex profile in its middle reaches between ~700-2000 m and less steep, concave profiles in its upper reaches above ~2000 m and lower reaches below ~700 m (Fig. 4a). This is also reflected in its χ-plot, which shows high channel steepness in its middle reaches and low channel steepness in its lower and upper reaches (Fig. 4b). The Anning River shows an apparent knickpoint at ~1450 m in its χ-plot separating the gentle upper reaches from steepened lower reaches (Fig. 4b). The changes in river channel slope do not correlate with changes in substrate lithologies. For example, the bedrock lithology in the steep reaches of the Dadu includes both sedimentary strata and granites (Fig. 4a), indicating no systematic impact of substrate erodibility on river morphology.

This different morphology between the Dadu and Anning Rivers indicates that there is no regional aligned knickpoints on these two rivers and that these two rivers do not respond to a common rock uplift history. Instead, it implies that the capture between the Dadu and Anning Rivers at the town of Shimian has caused a sudden increase in water discharge in the lower Dadu which has enhanced river incision along this segment, which has had sufficient time to equilibrate into a concave profile. Above the capture point, the river profile has been modified by the migrating incision wave initiated from the capture point, leading to a disequilibrium middle segment and an unaffected upper segment. This is further supported by the distribution of the millennial-scale erosion rates determined by cosmogenic ^{10}Be dating (Ouimet et al., 2009) which show relatively low erosion rates of ~0.1-0.2 mm/yr in the upper Dadu above ~2000 m, and rates of ~0.2-0.6 mm/yr below this elevation (Fig. 4a). The Anning River, having lost drainage area in its headwaters, is characterized by low channel steepness and thus slow erosion in its upper reaches. In contrast, the lower Anning, being fixed to a base level at the confluence with the Yangtze, retains its original, higher steepness and this lower reach grows upstream with time (Beeson and McCoy, 2019). We have not modeled this process, but there is a large knickpoint at 1450 m elevation that could represent this transition.

To simulate the transient response of the Dadu to capture, we constructed a 1-D numerical model for the lower and middle segments of the Dadu including the change in drainage area that occurred following redirection of the upper Dadu into the modern lower Dadu. River capture was simulated by initially separating the modern Dadu River profile into two independent river segments, one upstream and one downstream from the capture location (at Shimian) which we subsequently refer to as the upper paleo-Dadu-

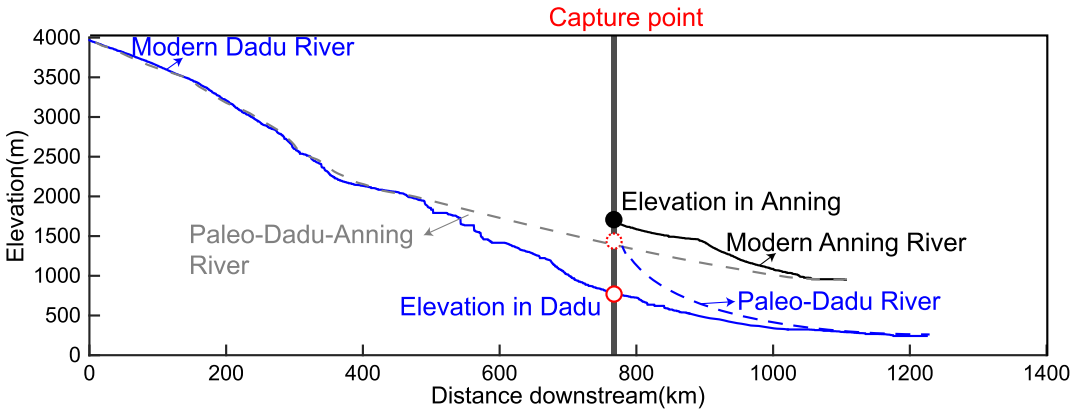

Fig. 5. Schematic of the model scenario for post-capture profile incision. The solid blue line indicates the modern Dadu River profile and the solid black line indicates the modern Anning River profile. The vertical bar represents the capture point. The closed red circle indicates the capture point at Shimian on the modern Dadu River and the solid black circle represents the elevation of the head of the modern Anning River. The dashed red circle is the elevation of the capture point at time of capture (a model parameter). The dashed grey line indicates the paleo-Dadu-Anning River and the dashed blue line indicates the paleo-Dadu River before capture. The upper section of the paleo-Dadu-Anning River above the capture point was connected with the paleo-Dadu River at time of capture and subsequently incised to the modern Dadu River profile. Note that the upper Anning profile is uplifted subsequent to capture as we assume incision rate drops to zero.

Anning and paleo-Dadu Rivers, respectively (Fig. 5). The drainage area at the capture point on the upstream profile was subtracted from all points on the downstream profile to estimate the drainage area of the paleo-Dadu River prior to the capture event. The pre-capture elevation at the capture point is unknown but we take the current elevation of the Anning River head as an approximation, correcting this downward by an assumed tectonic uplift since capture; this correction varies depending on the model uplift rate (Fig. 5). This assumes no erosion of the Anning head since capture. The simulation starts from a steady-state river profile before capture where rock uplift has been equilibrated with erosion and thus U is scaled with the channel steepness and rock erodibility (K). Two scenarios are investigated, in which (a) rock uplift rate is spatially uniform on both the upper paleo-Dadu-Anning and the paleo-Dadu Rivers and (b) rock uplift rate differs between these two rivers.

In both scenarios, we assume K is spatially uniform and varies between $1e^{-7}$ $m^{0.1}\,yr^{-1}$ and $1e^{-5}$ $m^{0.1}\,yr^{-1}$, which is within the range for most values of rock erodibility (Stock and Montgomery, 1999). Since our provenance analysis indicates that the river disruption of the paleo-Dadu-Anning River occurred after 2.6 Ma, we investigate potential time of capture on the range of 3 Ma to 0.1 Ma. For simplicity, we assume $n = 1$ for the main modeling analysis but simulations with both $n = 2/3$ and $n = 5/3$ are also presented in the supplement. In the uniform uplift scenario, uplift rate is spatially uniform along the river. In the non-uniform uplift rate scenario, we apply a rock uplift rate of U1 upstream of the capture point and a rate of U2 downstream of the capture point. Two values for the uplift rate are justified by the fact that the paleo-Dadu-Anning was largely following the Xianshuihe-Anninghe fault, whereas the paleo-Dadu runs roughly perpendicular to the fault. Thus, if rock uplift rate differs across this fault, the transition would occur near the capture point. In the model, we search over the parameters of K, time of capture, and uplift rate optimizing the fit to the current Dadu River profile. For each combination of parameters, the simulation starts at the time of capture and ends at present. Each model is evaluated by a misfit value which is taken as the sum of the absolute difference in the predicted and observed river elevations.

The results of this parameter space search are shown in Fig. 6 and Fig. 7. In both scenarios, the uplift rate and rock erodibility, K, covary, but are not completely dependent as U1 independently affects the starting elevation of the capture point. We investigate a range of U1 between 0.015 mm/yr and 1.53 mm/yr given the ranges of K and time of capture. The minimum misfit is reached with $K = 1.66e^{-6}$ $m^{0.1}\,yr^{-1}$, $U = 0.25$ mm/yr and $t = 1.6$ Ma, although there is a range of acceptable fits across parameter space for time of capture between 1.25 and 2.5 Ma (Fig. 6a). The uplift rate in the best-fit model is close to the ^{10}Be-based erosion rates in the unadjusted upper Dadu and the predicted profile from these parameters shows slightly higher elevation than the observed profile (Fig. 6b). In the non-uniform uplift scenario, U1 varies between 0.008 mm/yr and 2.78 mm/yr and U2 varies between 0.015 mm/yr and 1.53 mm/yr. The minimum misfit is found for $K = 1.14e^{-6}$ $m^{0.1}\,yr^{-1}$, U1 = 0.24 mm/yr, U2 = 0.17 mm/yr and $t = 2.4$ Ma (Fig. 7a). The uplift rate in the best-fit model is also close to the ^{10}Be constrained erosion rates in the unadjusted upper Dadu. Compared with the previous scenario, this scenario shows a better match between the predicted and observed river profiles (Fig. 7b). The capture between the Dadu and Anning Rivers at 2.4 Ma is also in good agreement with the time for changes in the provenance of the Anning river sediments. For this scenario, we also ran simulations with $n = 2/3$ and $n = 5/3$ while keeping the rest of the parameters the same as in the case of $n = 1$. For $n = 2/3$, the best-fit model predicts a river profile that is higher than the observed (Supplementary Data Fig. 1). For $n = 5/3$, the best-fit model shows a reasonable match with the observed profile (Supplementary Data Fig. 2) but the required uplift rate (U1) (>1 mm/yr) is much higher than the ^{10}Be derived erosion rates in the unaffected upper Dadu.

Our preferred scenario is consistent with post-capture incision rates and amounts derived from ^{10}Be data and thermochronometry. The total incision of the Dadu River is determined as the sum of the rock uplift and surface lowering accumulated since capture. Given a rock uplift rate of 0.24 mm/yr, a capture time of 2.4 Ma, and a maximum change in surface elevation of 300 m at the capture point as depicted on Fig. 7b, we obtained a maximum incision amount of ~876 m on the modern Dadu near the capture point at the town of Shimian. The ^{10}Be derived erosion rates between the capture point and 2000 m elevation imply an incision of ~480–1440 m during the last 2.4 Ma which is similar to that from the modeling. To calculate the incision amount from the thermochronometric ages, we used the analytical approach of Willett and Brandon (2013). This approach converts a thermochronometric age to a time-averaged exhumation rate during the time interval determined by the age. We calculated the exhumation from the AHe ages of sample DD05 and DD06 since these two samples were collected from low elevations close to the modern river bed and their AHe ages are close to the time of river capture, which would allow us to determine the maximum incision amount after capture. Parameters used for the calculation are in Supplementary

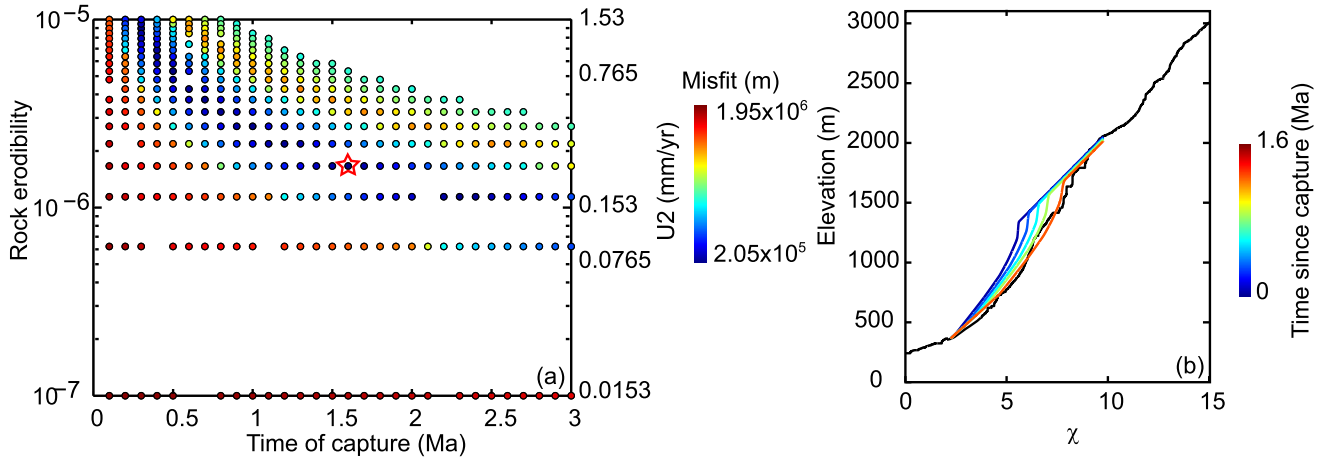

Fig. 6. Results for the single uplift value model. The misfit plot (a) and the predicted Dadu River χ-plot from the best-fit parameters (red star) and the current Dadu River χ-plot (b). Each circle in (a) indicates a simulation and the filled color of this circle denotes the misfit between the modeled Dadu River χ-plot at present and the observed profile. The red star shows the best model and has parameters of $K = 1.66e^{-6}$ $m^{0.1}\,yr^{-1}$, $U = 0.25$ mm/yr and time of capture at 1.6 Ma. The black line in (b) shows the modern Dadu River χ-plot and the colored lines show the evolution of the Dadu River profile following capture modeled with the lowest-misfit parameters with steps of 0.4 Ma.

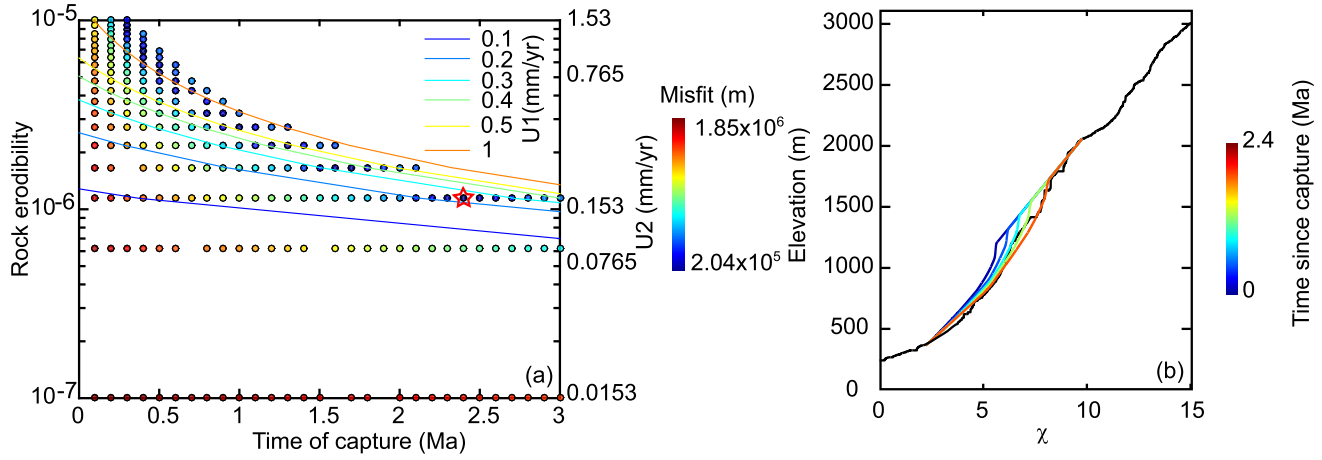

Fig. 7. Results for model of Dadu profile assuming two uplift rates, with change in uplift rate at the capture point. The misfit plot (a) and the predicted Dadu River χ-plot from the best-fit parameters and the observed profile (b). Each circle in (a) indicates a simulation and the filled color of this circle denotes the misfit between the modeled Dadu River χ-plot at present and the observed one. The red star shows the best model and has parameters of $K = 1.14e^{-6}$ $m^{0.1}\,yr^{-1}$, U1 = 0.24 mm/yr, U2 = 0.17 mm/yr and time of capture at 2.4 Ma. The black line in (b) shows the modern Dadu River χ-plot and the colored lines show the evolution of the Dadu River profile following capture modeled with the lowest-misfit parameters with steps of 0.6 Ma.

Data Table 6. We obtained an exhumation rate of ~0.9 km/Ma from sample DD06 and an exhumation rate of ~0.3 from sample DD05 which leads to a total exhumation estimate of ~720 m over the last 0.8 Ma and of ~870 m over the last 2.9 Ma, respectively. These estimates are consistent with a total incision amount of ~876 m in the last 2.4 Ma calculated from the modeling.

5. Cause of the Dadu-Anning capture and its regional implication

By combining the provenance analysis, incision history constrained from thermochronometry, and river analysis and numerical modeling, we suggest an Early Pleistocene capture of the upper Dadu from the modern Anning River, where the upper course of the paleo-Dadu-Anning River was captured by the paleo-Dadu, resulting in the modern Dadu River and beheading the modern Anning River. This capture has resulted in changes of the sediment source of the Anning, enhanced river incision and a transient profile of the Dadu River. Previous studies suggested that changes in drainage pattern in eastern Tibet are a response to the regional surface uplift (Clark et al., 2004; Clift et al., 2006) or regional shortening (Hallet and Molnar, 2001). However, the Dadu-Anning capture postdates the Late Miocene uplift in eastern Tibet. Rather, we suggest that the Dadu-Anning capture is associated with movement of the local Daliangshan fault. This fault was active at ~3 Ma (An et al., 2008), which is coeval with the Anning-Dadu river capture, and has caused a total offset of ~11 km and a ~7 km sinistral deflection of the lower Dadu River course (He and Oguchi, 2008). It is possible that this displacement disconnected the upper paleo-Dadu-Anning River from its lower reaches, leading to the reorganization of the channel networks.

In the eastern Tibetan Plateau, onset of rapid river incision has been used as a proxy for the timing of plateau uplift (Clark et al., 2005; Ouimet et al., 2010). However, incision can also be enhanced by river capture due to lateral movement of local faults. In this case, initiation of rapid incision does not pinpoint the time for plateau uplift. Along other major rivers in the eastern Tibetan Plateau, segmentation of rivers by strike-slip faults are frequent (Burchfiel and Wang, 2003; Wang and Burchfiel, 2000). Similar to the Dadu-Anning capture, incision along rivers can also be enhanced due to river network disruption. Across the eastern Tibetan Plateau, the onset of increased incision along different courses of the major rivers is spread over an extended time span. For ex-

ample, onsets of rapid incision were dated from 8-7 Ma to 35-30 Ma along the Yalong River and its tributaries (Ouimet et al., 2010; Wang et al., 2012; Zhang et al., 2016), and from 20∼10 Ma to >20-30 Ma along the Yangtze River (Mcphillips et al., 2015; Ouimet et al., 2010; Shen et al., 2016; Tian et al., 2014) (Fig. 1a). Such variations in the commencement of increased incision along rivers are too large to be regarded as a lag time from a migrating incision wave in response to regional surface uplift, which usually propagates fast along large rivers (Whipple and Tucker, 1999). Instead, such variations may either reflect variations in the surface uplift history or disruptions caused by stream network reorganization. In addition, gradual drainage network expansion in response to surface uplift, for example, as recorded by the Pearl River in the southeastern Tibetan Plateau (Cao et al., 2018), can also trigger delayed river incision in upstream reaches which may also complicate the determination of the time of tectonic uplift.

6. Summary and conclusions

We present several new lines of evidence for the capture of the headwaters of an earlier Anning River into the modern Dadu from provenance analysis, thermochronometry, topographic analysis and numerical modeling of the river profile.

Our provenance analysis reveals contrasting detrital zircon U-Pb age patterns for the modern Dadu and modern Anning where the former is dominated by a prominent Triassic peak and a small Neoproterozoic peak while the latter shows the opposite pattern with a dominance of Neoproterozoic ages over Triassic ages. The Pliocene Xigeda formation, distributed along the modern Anning River, shows an age spectrum similar to the modern Dadu River, indicating a paleo-connection between the Anning and the Dadu during the deposition of this formation. Our bedrock thermochronometric data reveal rapid cooling since ∼10 Ma and a suggestion of accelerated cooling at ∼2 Ma. While the former cooling period is associated with the regional uplift, the latter may reflect enhanced river incision due to river capture from the Anning into the Dadu. Consistent with the provenance analysis and thermochronometry, our topographic analysis and numerical modeling also suggest the Early Pleistocene Dadu-Anning capture occurred at ∼2.4 Ma. We infer that the Dadu-Anning capture is associated with the left-lateral movement of the Daliangshan fault. Our results also imply that impulsive, rapid incision can be caused by river capture, associated with strike-slip faulting, so that caution must be taken when using river incision as a proxy for tectonic uplift of features such as the Tibetan plateau.

Acknowledgements

This project was supported by National Natural Science Foundation of China (41720104003, 41602210) and the Fundamental Research Funds for the Central Universities (2018XZZX001-03) to R.Y. L.G. was supported by ETH postdoctoral fellowship (FEL-11 15-2). We thank Shaomei Yang and Shenqiang Chen for their assistance with the thermochronometric dating.

Appendix A. Supplementary material

Supplementary material related to this article can be found online at https://doi.org/10.1016/j.epsl.2019.115955.

References

An, Y., Han, Z., Wan, J., 2008. Fission track dating of the Cenozoic uplift in Mabian area, southern Sichuan Province, China. Sci. China, Ser. D, Earth Sci. 51, 1238–1247.

Barbour, G.B., 1936. Physiographic history of the Yangtze. Geogr. J. 87, 17–32.

Beeson, H.W., McCoy, S.W., 2019. Geomorphic signatures of the transient fluvial response to tilting. Earth Surf. Dyn. Discuss., 1–39.

Brookfield, M., 1998. The evolution of the great river systems of southern Asia during the Cenozoic India-Asia collision: rivers draining southwards. Geomorphology 22, 285–312.

Burchfiel, B., Wang, E., 2003. Northwest-trending, middle Cenozoic, left-lateral faults in southern Yunnan, China, and their tectonic significance. J. Struct. Geol. 25, 781–792.

Burchfiel, B.C., Chen, Z., 2012. Tectonics of the Southeastern Tibetan Plateau and Its Adjacent Foreland. Geological Society of America.

Cao, L., Shao, L., Qiao, P., Zhao, Z., van Hinsbergen, D.J.J.E., Letters, P.S., 2018. Early miocene birth of modern Pearl River recorded low-relief, high-elevation surface formation of SE Tibetan Plateau. Earth Planet. Sci. Lett. 496, 120–131.

Cao, K., Wang, G., Leloup, P.H., Mahéo, G., Xu, Y., van der Beek, P.A., Replumaz, A., Zhang, K.J.T., 2019. Oligocene-Early Miocene topographic relief generation of southeastern Tibet triggered by thrusting. Tectonics 38, 374–391.

Cawood, P.A., Nemchin, A.A., Freeman, M., Sircombe, K., 2003. Linking source and sedimentary basin: detrital zircon record of sediment flux along a modern river system and implications for provenance studies. Earth Planet. Sci. Lett. 210, 259–268.

Clark, M.K., House, M.A., Royden, L.H., Whipple, K.X., Burchfiel, B.C., Zhang, X., Tang, W., 2005. Late Cenozoic uplift of southeastern Tibet. Geology 33, 525–528.

Clark, M.K., Schoenbohm, L.M., Royden, L.H., Whipple, K.X., Burchfiel, B.C., Zhang, X., Tang, W., Wang, E., Chen, L., 2004. Surface uplift, tectonics, and erosion of eastern Tibet from large-scale drainage patterns. Tectonics 23, TC1006.

Clift, P.D., Blusztajn, J., Nguyen, A.D., 2006. Large-scale drainage capture and surface uplift in eastern Tibet–SW China before 24 Ma inferred from sediments of the Hanoi Basin, Vietnam. Geophys. Res. Lett. 33, L19403.

Ding, L., Yang, D., Cai, F.L., Pullen, A., Kapp, P., Gehrels, G.E., Zhang, L.Y., Zhang, Q.H., Lai, Q.Z., Yue, Y.H., Shi, R.D., 2013. Provenance analysis of the Mesozoic Hoh-Xil-Songpan-Ganzi turbidites in northern Tibet: implications for the tectonic evolution of the eastern Paleo-Tethys Ocean. Tectonics 32, 34–48.

Enkelmann, E., Weislogel, A., Ratschbacher, L., Eide, E., Renno, A., Wooden, J., 2007. How was the Triassic Songpan-Ganzi basin filled? A provenance study. Tectonics 26, TC4007.

Gallagher, K., 2012. Transdimensional inverse thermal history modeling for quantitative thermochronology. J. Geophys. Res., Solid Earth 117, B02408. https://doi.org/10.1029/2011JB008825.

Godard, V., Pik, R., Lavé, J., Cattin, R., Tibari, B., de Sigoyer, J., Pubellier, M., Zhu, J., 2009. Late Cenozoic evolution of the central Longmen Shan, eastern Tibet: insight from (U-Th)/He thermochronometry. Tectonics 28, TC5009.

Gourbet, L., Leloup, P.H., Paquette, J.-L., Sorrel, P., Maheo, G., Wang, G., Yadong, X., Cao, K., Antoine, P.-O., Eymard, I., Liu, W., Lu, H., Replumaz, A., Chevalier, M.-L., Kexin, Z., Jing, W., Shen, T., 2017. Reappraisal of the Jianchuan Cenozoic basin stratigraphy and its implications on the SE Tibetan plateau evolution. Tectonophysics 700–701, 162–179.

Guenthner, W.R., Reiners, P.W., Ketcham, R.A., Nasdala, L., Giester, G., 2013. Helium diffusion in natural zircon: radiation damage, anisotropy, and the interpretation of zircon (U-Th)/He thermochronology. Am. J. Sci. 313, 145–198.

Hallet, B., Molnar, P., 2001. Distorted drainage basins as markers of crustal strain east of the Himalaya. J. Geophys. Res., Solid Earth (1978–2012) 106, 13697–13709.

He, H., Oguchi, T., 2008. Late Quaternary activity of the Zemuhe and Xiaojiang faults in southwest China from geomorphological mapping. Geomorphology 96, 62–85.

He, M., Zheng, H., Bookhagen, B., Clift, P.D., 2014. Controls on erosion intensity in the Yangtze River basin tracked by U–Pb detrital zircon dating. Earth-Sci. Rev. 136, 121–140.

Howard, A.D., 1994. A detachment-limited model of drainage basin evolution. Water Resour. Res. 30, 2261–2285.

Huang, X.-L., Xu, Y.-G., Lan, J.-B., Yang, Q.-J., Luo, Z.-Y., 2009. Neoproterozoic adakitic rocks from Mopanshan in the western Yangtze Craton: partial melts of a thickened lower crust. Lithos 112, 367–381.

Jiang, F., Wu, X., Xiao, H., Zhao, Z., 1999. On the age of the Xigeda formation in Luding, Sichuan, and its Neotectonic significance. Acta Geol. Sin. 73, 1–6 (in Chinese with English abstract).

Kirby, E., Reiners, P.W., Krol, M.A., Whipple, K.X., Hodges, K.V., Farley, K.A., Tang, W., Chen, Z., 2002. Late Cenozoic evolution of the eastern margin of the Tibetan Plateau: inferences from $^{40}Ar/^{39}Ar$ and (U-Th)/He thermochronology. Tectonics 21, TC1246.

Kong, P., Granger, D., Wu, F., Caffee, M., Wang, Y., Zhao, X., Zheng, Y., 2009. Cosmogenic nuclide burial ages and provenance of the Xigeda paleo-lake: implications for evolution of the Middle Yangtze River. Earth Planet. Sci. Lett. 278, 131–141.

Kong, P., Zheng, Y., Caffee, M.W., 2012. Provenance and time constraints on the formation of the first bend of the Yangtze River. Geochem. Geophys. Geosyst. 13, Q06017.

Mcphillips, D., Hoke, G.D., Liu-Zeng, J., Bierman, P.R., Rood, D.H., Niedermann, N., 2015. Dating the incision of the Yangtze River gorge at the First Bend using three-nuclide burial ages. Geophys. Res. Lett. 42. https://doi.org/10.1002/2015GL066780.

Ouimet, W.B., Whipple, K.X., Granger, D.E., 2009. Beyond threshold hillslopes: channel adjustment to base-level fall in tectonically active mountain ranges. Geology 37, 579–582.
Ouimet, W., Whipple, K., Royden, L., Reiners, P., Hodges, K., Pringle, M., 2010. Regional incision of the eastern margin of the Tibetan Plateau. Lithosphere 2, 50–63.
Perron, J.T., Royden, L., 2012. An integral approach to bedrock river profile analysis. Earth Surf. Process. Landf. 38, 570–576.
Qian, F., Xu, S., Chen, F., Zhao, Y., 1984. Study on the paleomagnetism of the Xigeda formation. Mount. Res. 2, 275–282.
Roger, F., Calassou, S., Lancelot, J., Malavieille, J., Mattauer, M., Zhiqin, X., Ziwen, H., Liwei, H., 1995. Miocene emplacement and deformation of the Konga Shan granite (Xianshui He fault zone, west Sichuan, China): geodynamic implications. Earth Planet. Sci. Lett. 130, 201–216.
Roger, F., Malavieille, J., Leloup, P.H., Calassou, S., Xu, Z., 2004. Timing of granite emplacement and cooling in the Songpan–Garzê Fold Belt (eastern Tibetan Plateau) with tectonic implications. J. Asian Earth Sci. 22, 465–481.
SBGMR (Sichuan Bureau of Geology and Mineral Resources), 1991. Regional Geology of Sichuan Province. Geological Publishing House, Beijing. Scale 1:200000, 1 sheet.
Shen, W., Li, H., Xu, S., Wang, R., 2000. U-Pb chronological of zircons from the Huangcaoshan and Xiasuozi granites in the western margin of Yangtze Plate. Geol. J. Chin. Univ. 6, 412–416 (in Chinese with English abstract).
Shen, X., Tian, Y., Li, D., Qin, S., Vermeesch, P., Schwanethal, J., 2016. Oligocene-Early Miocene river incision near the first bend of the Yangze River: insights from apatite (U-Th-Sm)/He thermochronology. Tectonophysics 687, 223–231.
Stock, J.D., Montgomery, D.R., 1999. Geologic constraints on bedrock river incision using the stream power law. J. Geophys. Res., Solid Earth (1978–2012) 104, 4983–4993.
Sun, W.-H., Zhou, M.-F., Gao, J.-F., Yang, Y.-H., Zhao, X.-F., Zhao, J.-H., 2009. Detrital zircon U–Pb geochronological and Lu–Hf isotopic constraints on the Precambrian magmatic and crustal evolution of the western Yangtze Block, SW China. Precambrian Res. 172, 99–126.
Tian, Y., Kohn, B.P., Gleadow, A.J.W., Hu, S., 2013. Constructing the Longmen Shan eastern Tibetan Plateau margin: insights from low-temperature thermochronology. Tectonics 32, 576–592.
Tian, Y., Kohn, B.P., Gleadow, A.J.W., Hu, S., 2014. A thermochronological perspective on the morphotectonic evolution of the southeastern Tibetan Plateau. J. Geophys. Res., Solid Earth 119, 676–698.
Tian, Y., Kohn, B.P., Hu, S., Gleadow, A.J.W., 2015. Synchronous fluvial response to surface uplift in the eastern Tibetan Plateau: implications for crustal dynamics. Geophys. Res. Lett. 42, 29–35.
Tucker, G.E., Whipple, K.X., 2002. Topographic outcomes predicted by stream erosion models: sensitivity analysis and intermodel comparison. J. Geophys. Res., Solid Earth 107, 2179. https://doi.org/10.1029/2001JB000162.
Wang, E., Burchfiel, B.C., 2000. Late Cenozoic to Holocene deformation in southwestern Sichuan and adjacent Yunnan, China, and its role in formation of the southeastern part of the Tibetan Plateau. Geol. Soc. Am. Bull. 112, 413–423.
Wang, S., Zhao, Z., Qiao, Y., Jiang, F., 2006. Age and paleoenvironment of Xigeda Formation in Luding, Sichuan. Q. Sci. 26, 257–264.
Wang, S., Jiang, G., Xu, T., Tian, Y., Zheng, D., Fang, X., 2012. The Jinhe–Qinghe fault—an inactive branch of the Xianshuihe–Xiaojiang fault zone, Eastern Tibet. Tectonophysics 544–545, 93–102.
Wei, H.-H., Wang, E., Wu, G.-L., Meng, K., 2016. No sedimentary records indicating southerly flow of the paleo-Upper Yangtze River from the First Bend in southeastern Tibet. Gondwana Res. 32, 93–104.
Weislogel, A.L., Graham, S.A., Chang, E.Z., 2006. Detrital zircon provenance of the Late Triassic Songpan-Ganzi complex: sedimentary record of collision of the North and South China blocks. Geology 34, 97–100.
Whipple, K.X., Tucker, G.E., 1999. Dynamics of the stream-power river incision model: implications for height limits of mountain ranges, landscape response timescales, and research needs. J. Geophys. Res., Solid Earth (1978–2012) 104, 17661–17674.
Whipple, K.X., Hancock, G.S., Anderson, R.S., 2000. River incision into bedrock: mechanics and relative efficacy of plucking, abrasion, and cavitation. Geol. Soc. Am. Bull. 112, 490–503.
Willett, S.D., Brandon, M.T., 2013. Some analytical methods for converting thermochronometric age to erosion rate. Geochem. Geophys. Geosyst. 14, 209–222.
Wilson, C.J.L., Fowler, A.P., 2011. Denudational response to surface uplift in east Tibet: evidence from apatite fission-track thermochronology. Geol. Soc. Am. Bull. 123, 1966–1987.
Xu, G., Kamp, P.J., 2000. Tectonics and denudation adjacent to the Xianshuihe Fault, eastern Tibetan Plateau: constraints from fission track thermochronology. J. Geophys. Res., Solid Earth (1978–2012) 105, 19231–19251.
Xu, Y.-G., Luo, Z.-Y., Huang, X.-L., He, B., Xiao, L., Xie, L.-W., Shi, Y.-R., 2008. Zircon U–Pb and Hf isotope constraints on crustal melting associated with the Emeishan mantle plume. Geochim. Cosmochim. Acta 72, 3084–3104.
Yan, Y., Carter, A., Huang, C.-Y., Chan, L.-S., Hu, X.-Q., Lan, Q., 2012. Constraints on Cenozoic regional drainage evolution of SW China from the provenance of the Jianchuan Basin. Geochem. Geophys. Geosyst. 13, Q11008.
Yang, R., Willett, S.D., Goren, L., 2015. In situ low-relief landscape formation as a result of river network disruption. Nature 520, 526–529.
Yanites, B.J., Ehlers, T.A., Becker, J.K., Schnellmann, M., Heuberger, S., 2013. High magnitude and rapid incision from river capture: Rhine River, Switzerland. J. Geophys. Res., Earth Surf. 118, 1060–1084.
Yao, H., Zhao, Z., Qiao, Y., Li, C., Wang, S., Wang, Y., Chen, Y., Jiang, F., 2007. Magnetostratigraphic dating of the Xigeda formation in Mianning, Sichuan and its significance. Q. Sci. 27, 74–84.
Yuan, C., Zhou, M.-F., Sun, M., Zhao, Y., Wilde, S., Long, X., Yan, D., 2010. Triassic granitoids in the eastern Songpan Ganzi Fold Belt, SW China: magmatic response to geodynamics of the deep lithosphere. Earth Planet. Sci. Lett. 290, 481–492.
Zhang, H.-F., Zhang, L., Harris, N., Jin, L.-L., Yuan, H., 2006. U–Pb zircon ages, geochemical and isotopic compositions of granitoids in Songpan-Garze fold belt, eastern Tibetan Plateau: constraints on petrogenesis and tectonic evolution of the basement. Contrib. Mineral. Petrol. 152, 75–88.
Zhang, H., Oskin, M.E., Liu-Zeng, J., Zhang, P., Reiners, P.W., Xiao, P., 2016. Pulsed exhumation of interior eastern Tibet: implications for relief generation mechanisms and the origin of high-elevation planation surfaces. Earth Planet. Sci. Lett. 449, 176–185.
Zhang, Y., Replumaz, A., Leloup, P.H., Wang, G.-C., Bernet, M., van der Beek, P., Paquette, J.L., Chevalier, M.-L., 2017a. Cooling history of the Gongga batholith: implications for the Xianshuihe Fault and Miocene kinematics of SE Tibet. Earth Planet. Sci. Lett. 465, 1–15.
Zhang, P., Najman, Y., Mei, L., Millar, I., Sobel, E.R., Carter, A., Barfod, D., Dhuime, B., Garzanti, E., Govin, G., Vezzoli, G., Hu, X., 2019. Palaeodrainage evolution of the large rivers of East Asia, and Himalayan-Tibet tectonics. Earth-Sci. Rev. 192, 601–630.
Zhang, Z., Daly, J.S., Li, C.A., Tyrrell, S., Sun, X., Yan, Y., 2017b. Sedimentary provenance constraints on drainage evolution models for SE Tibet: evidence from detrital K-feldspar. Geophys. Res. Lett. 44, 4064–4073.
Zhao, J.H., Zhou, M.F., 2007. Neoproterozoic adakitic plutons and arc magmatism along the western margin of the Yangtze Block, South China. J. Geol. 115, 675–689.
Zhou, M.-F., 2002. SHRIMP U-Pb zircon geochronological and geochemical evidence for Neoproterozoic arc-magmatism along the western margin of the Yangtze Block, South China. Earth Planet. Sci. Lett. 196, 51–67.